Journal of Electroceramics
https://doi.org/10.1007/s10832-021-00248-5

Electrical and structural properties of new type Er and Yb doped bismuth oxide solid electrolytes synthesized by Pechini method

Senel Cobaner[1] · Serdar Yilmaz[2,3]

Received: 23 July 2019 / Accepted: 15 June 2021

Abstract
In this study Bismuth-based nano-sized powders have been synthesized with Sol-Gel Pechini method by doping Er^{3+} and Yb^{3+}. The microstructural and electrical properties were characterized and discussed in detail. The fcc cubic structures (δ-phase) were successfully obtained at 700, 750 and 800 °C. With the increase in sintering temperature, the range of cubic boundary values decreased. The lattice parameter decreased independently of the temperature with the increasing total dopant ratio. Total dopant rate should be minimum 18 mol%, respectively to obtain the δ-phase at 700 °C sintering temperature. On the other hand, dopant amounts of Er and Yb cations should be at a certain value. Total electrical conductivity was measured under various temperature conditions and doping concentration and Activation energies belong to samples are calculated. At the intermediate temperature zone (selected as 510 °C) the conductivity values were decreased with the increasing total dopant ratio. Conversely, the conductivity values were increased with the increasing total dopant ratio in the high-temperature region. Activation energies of cubic samples were measured as around ~0.9–1.3 eV.

Keywords Bismuth based Electroceramics · Structural properties · Electrical properties · Pechini method · Peak shift

1 Introduction

Electrolytes, an important component of solid oxide fuel cells, have a dense and high oxygen ion conductivity [1]. Bismuth oxide-based systems, face-centred cubic phase via lanthanide doping regime, has one of the highest oxygen-ion conductivities among all solid oxide electrolytes [2]. To obtain a high concentration of charge carriers, the fluorite oxides are doped with either divalent or trivalent cations [1].

Due to the highly anionic conductivity properties, Bismuth-based solid electrolytes are used in industry in the production process of some solid oxide electrolytes and membranes and the production of electrochemical cells [3, 4]. Monoclinic phase (α-Bi_2O_3), bcc phase (γ-Bi_2O_3), *fcc* phase (δ-Bi_2O_3), and tetragonal (β-Bi_2O_3) phase are intensely studied four phases of Bi_2O_3 out of its six crystal modifications [5]. Oxygen ionic conductivity of the monoclinic α-Bi_2O_3 phase, tetragonal β-Bi_2O_3, body centred cubic γ-Bi_2O_3 phases is lower than that of the face-centred cubic δ-Bi_2O_3 phase structure [5–7]. At lower temperatures, the work on the production and characterization of new electrolytes with higher oxygen ionic conductivity and dissociation maintains an update [7]. δ-Bi_2O_3 has high oxygen ionic conductivity due to its defective fluoride (CaF_2) type crystal structure and high oxygen ion vacancies [8].

In recent years, Jaiswal et al. have investigated that $Bi_{0.80}Er_{0.20}O_{1.5}$ (ESB) have been prepared by using citrate–nitrate auto combustion method [2]. It is found that addition of ESB increases the conductivity of the bulk as well as of grain boundaries among all stabilized Bi_2O_3 systems, $(Er_2O_3)_x(Bi_2O_3)_{1-x}$ binary system has the highest conductivity at $x = 20$ mol% concentration [9, 10]. Verkerk et al. showed that $(Bi_2O_3)_{0.80}(Er_2O_3)_{0.20}$ had an ionic conductivity of 0.023 Scm^{-1} at 500 °C and 0.37 Scm^{-1} at 700 °C [11]. Torun et al. observed that the maximum level of the electrical conductivity for δ-phase $(Bi_2O_3)_{0.84}(Yb_2O_3)_{0.16}$ binary system was 0.316 Scm^{-1} and 0.632 Scm^{-1} sintered samples at 700 °C and 750 °C, respectively for 48 h [12]. The modified version of the sol-gel method is called as Pechini method [13–15]. High purity product is a commonly used method because of being

✉ Serdar Yilmaz
syilmaz@mersin.edu.tr

[1] Department of Nanotechnology and Advanced Materials, Mersin University, Mersin, Turkey

[2] Department of Physics, Mersin University, Mersin, Turkey

[3] Department of Chemical and Process Engineering, University of Surrey, Guildford, UK

Published online: 24 June 2021

easy to control, with high homogeneity and low sintering temperature, a simple and effective method [15–17]. Pechini method based on the polymerisation of metal salts [15, 18].

In this study, the crystal structure and electrical conductivity properties of Erbium and Ytterbium-doped Bismuth Oxide ternary systems in $(Er_2O_3)_x(Yb_2O_3)_y(Bi_2O_3)_{1-x-y}$ simple formula (called by *x*E*y*YbSB) with $x = 4,8,12$ mol% and $y = 10,20,30$ mol% is investigated by sol-gel Pechini method. The effect of dopant ratio on the stabilization of δ-phase *x*E*y*YbSB ternary systems was analysed by XRD analysis. The grain formation, thermal stability and conductivity properties are performed via scanning electron microscopy (SEM), differential thermal analysis (DTA), thermal gravimetric analysis (TGA) and four-point probe electrical conductivity measurement 4PPT methods (4PPT), respectively. Nevertheless, the synthesizing of this ternary system and also synthesis method has not been reported until now. Therefore, dope rates were decided by looking at the studies of $(Yb_2O_3)_x(Bi_2O_3)_{1-x}$ ($x = 11–20$ mol%) [12] and $(Er_2O_3)_x(Bi_2O_3)_{1-x}$ ($x = 15–40$ mol%) [1, 11] binary compounds. In this study, Erbium and Ytterbium were used to better understand the effect of dopant concentration on ionic conductivity.

2 Materials and methods

2.1 Preparation of materials

Polycrystalline powders of *x*E*y*YbSB compounds were prepared under identical conditions via the sol–gel-based Pechini method. The starting materials $Er(NO_3)_3{\cdot}5H_2O$ (%99.9, Alfa Aesar) and $Yb(NO_3)_3{\cdot}5H_2O$ (%99.9, Alfa Aesar) compounds were doped into $Bi(NO_3)_3{\cdot}5H_2O$ (%99.99 Sigma Aldrich). The mole ratios and sample codes are shown in Table 1. Firstly, stoichiometric amounts of analytical grade $Er(NO_3)_3{\cdot}5H_2O$, $Yb(NO_3)_3{\cdot}5H_2O$, $Bi(NO_3)_3{\cdot}5H_2O$ were dissolved in a citric acid solution to which ethylene glycol and diluted nitric acid were added to obtain gel form. The gel was dried at 120 °C for 12 h in an incubator to obtain a resin, grounded in an agate mortar and calcined at 500 °C for the burn-out the additives. The calcination temperature was determined according to the TGA analysis results described in the result section. Then the powders were sintered 700, 750 and 800 °C for 48 h in air, respectively. The sintering temperatures were determined from the literature survey [1, 11, 12].

2.2 Crystal structure and thermal analysis

XRD analysis (Rigaku Smartlab) was performed for identifying of the crystal structure and lattice parameters of synthesized powder materials. The analysis conditions have been applied with these parameters; scanned by 0.02 step width, $7° \le 2\theta \le 90°$ angular range and 21.6746 deg/min scanning speed at room temperature. The diffracted beams were counted with a 1D silicon strip detector (D/teX Ultra 250). XRD patterns were indexed and lattice parameter was calculated for every sample by PDXL2 software and using DICVOL06 method. XRD patterns were indexed and lattice parameter was calculated for every sample by PDXL2 software and DICVOL06 method. After the manual indexing process and determining the crystal structures of the samples, the lattice parameters are calculated by the software.

The thermal stability of the samples and the burning out temperature of the additives was investigated by DTA/TGA system (Perkin Elmer). The analyses were carried out with a heating rate of 10 °C/min, from the room temperature to 900 °C. Measurements were performed under the dynamic air atmosphere using a platinum sample holder and using the α-Al_2O_3 inert reference substance.

2.3 Microstructure characterization

The δ-phase powders were ball milled by the planetary ball mill (Retsch, PM100CM) at 500 rpm for 15 min in ethanol

Table 1 Observed phases and lattice parameters of δ-phase *x*E*y*YbSB ternary systems

Samples (*x*E*y*YbSB)	*x* (mol%)	*y* (mol%)	Total (mol%)	Sintering Temperature		
				700 °C	750 °C	800 °C
4E10YbSB	4	10	14	*β*	*β*	*β*
8E10YbSB	8	10	18	*δ (5.5090 Å)*	*δ (5.5077 Å)*	*δ (5.5060 Å)*
12E10YbSB	12	10	22	*δ (5.5032 Å)*	*δ (5.5018 Å)*	*δ (5.5009 Å)*
4E20YbSB	4	20	24	δ (5.4905 Å)	δ (5.5042 Å)	δ (5.4896 Å)
8E20YbSB	8	20	28	*δ (5.4791 Å)*	*δ (5.4803 Å)*	*δ (5.4795 Å)*
12E20YbSB	12	20	32	*δ (5.4661 Å)*	*δ (5.4679 Å)*	*δ (5.4672 Å)*
4E30YbSB	4	30	34	δ (5.4530 Å)	δ (5.4537 Å)	α + δ
8E30YbSB	8	30	38	δ (5.4402 Å)	δ (5.4406 Å)	α + δ
12E30YbSB	12	30	42	δ (5.4313 Å)	α + δ	α

with agate ball media and then they were dried in the incubator. To determinate the optimized pressure level, cubic powder samples were pelletized by the single axial hydraulic press under different pressure levels of each one at 20 MPa, 75 MPa and 100 MPa with 1 mm thickness and 13 mm diameter. Then the pellets were calcined at 800 °C temperature for 48 h on a platinum substrate in air. Surface analyses of pellet samples were performed by SEM (ZEISS SUPRA55, Oberkochen, Germany).

2.4 Conductivity measurements

Resistance measurements were performed to circular samples using standard Four-Point Probe d.c. the technique (4PPT) under several temperature conditions for comparing the all fcc-phase samples each other. The total conductivities of samples were calculated using the resistance and geometric dimensions of sample and these data were only used for the comparing and determining the Activation Energies. The fcc phase powder samples were pressed into pellets with ~0.1 cm thickness (t) and 1.3 cm diameter (d) under 100 MPa pressure. The probes were directly contacted on a sample surface and adhesive paste was not used. The contacts were positioned symmetrically on the centre of the circular pellets. The resistance measurements performed from 300 °C to 820 °C temperature. The heating rate was applied to 5 °C/min and was held for 15 min at each 50 °C steps for thermal stability. During the measurements, the sample temperature was determined by a thermocouple, 5 mm away from the sample.

3 Results and discussion

3.1 Structural and thermal analysis

Observed phases and dopant rates of xEyYbSB ternary systems can be seen in Table 1. In this ternary system, the fcc cubic phases (δ-phase) were observed at 700, 750 and 800 °C. As seen in Table 1, the mixed phases occurred with the increasing sintering temperature. To obtain the δ-phase xEyYbSB system, the minimum sintering temperature should be at 700 °C. The cubic phase formation was seen in the total dopant ratio as $18 \leq x + y \leq 42$ for 700 °C sintering temperature. When the sintering temperature increased, additive range decreased to $18 \leq x + y \leq 38$ for 750 °C and $18 \leq x + y \leq 32$ for 800 °C sintering temperature (Table 1). Hereby, as the sintering temperature increases, the dopant mole range of cubic boundary values decrease It is seen in the XRD pattern (Fig. 1a and b) that the cubic structure is distorted as the sintering temperature increases. Similar features are observed in the other samples. The peaks seen in the XRD patterns of the secondary phases were only observed some of the samples sintered at 800 °C. The observed secondary phases in Fig. 1a and b belong to monoclinic phases for the samples sintered at 800 °C. As seen in Table 1, these samples exhibited the fcc

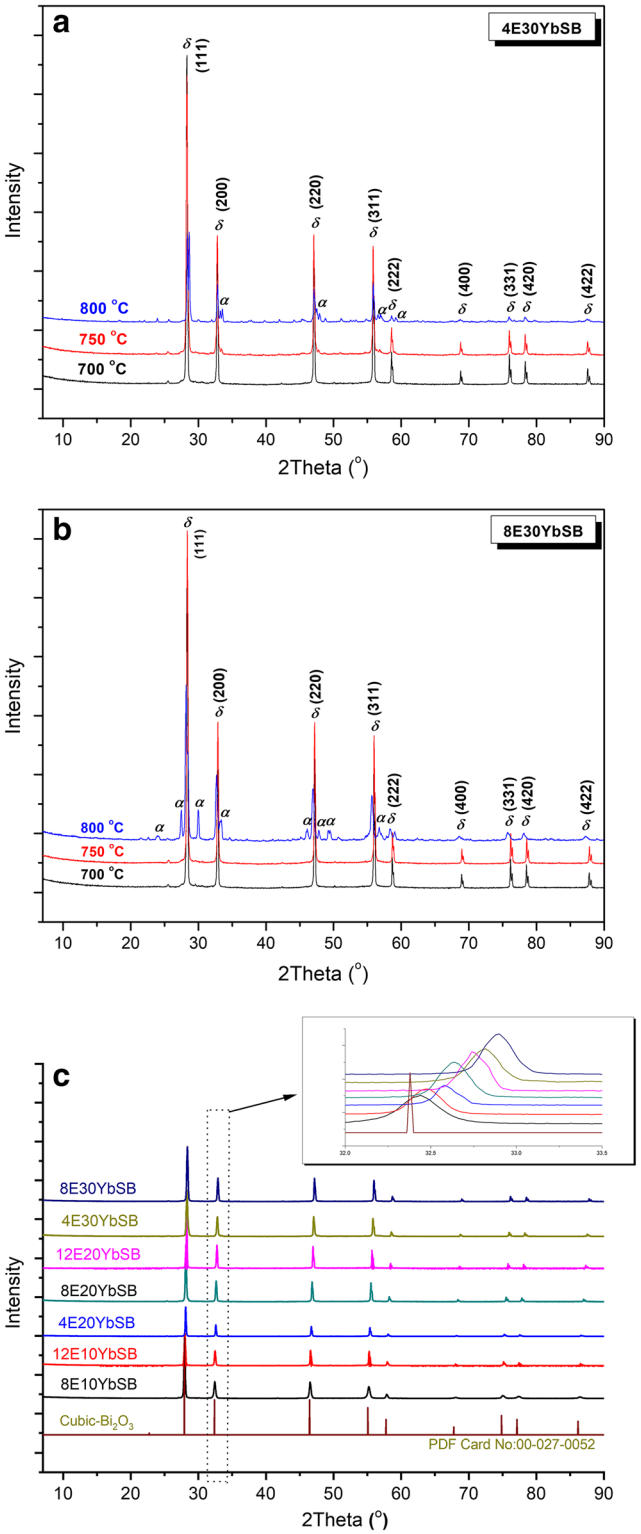

Fig. 1 XRD pattern of (**a**) 4E30YbSB, (**b**) 8E30YbSB samples at different sintering temperatures and (**c**) all of the cubic samples at sintered at 750 °C and with a magnified version of $2\theta = 31° - 34°$

and monoclinic mixed phases at the 800 °C sintering temperature and the peaks belong to these phases were pointed in the Fig.1a and b.

As well as total dopant ratio, dopant rate of each dopant cations is also important. The relationship between dopant amount and phase formation can be seen in Fig. 2 phase distribution map. It is clearly seen that the total dopant rate should be minimum 18 mol% and more to obtain fcc phase for *x*E*y*YbSB ternary system sintered at 700 °C. Therefore Er^{3+} and Yb^{3+} dopant rate should also be minimum 8 and 10 mol%, respectively, for 18 mol% stoichiometric composition. According to the result, the Er^{3+} dopant rate should be increased while the Yb^{3+} rate decreases and the total doping rate should be constant at a certain ratio to obtain fcc-phases. In a study conducted by Özlü Torun et al., it was reported that Yb dopant should be a minimum of 14 mol% for the cubic phase [12]. On the other hand, in this study, it was required a higher sintering temperature (800 °C) for 17 mol% and more dopant ratio to obtain the cubic phase (Fig. 2) and minimum dopant rate was found as 18 mol% at 700 °C sintering temperature to obtain fcc phase [12]. Although the cubic phase was obtained in the literature with less dopant, in this study the lower sintering temperature was enough despite the higher dopant rate. The main reason for the requirement of the low sintering temperature required was thought to be the sol-gel Pechini method. The low sintering temperature (700 °C) is enough to obtain a cubic phase, which is an important result in terms of production cost.

For evaluating the relations between the cation dopant rates and scattering angles taken from XRD patterns, each peak position ($2\theta_n$ angles) in XRD patterns of our samples were compared with peak angles of the pure δ-phase Bi_2O_3 ($2\theta_{Bi}$) taken from XRD pattern PDF card [19]. The differences between the two peak angles were calculated with the $2\theta_n$-$2\theta_{Bi}$ equation and called as "peak shift" and numbered in Table 2.

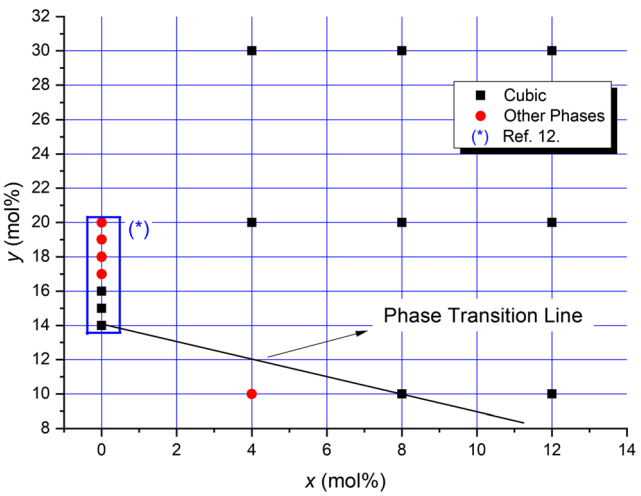

Fig. 2 The phase distribution graph of powder samples sintered for 48 h at 700 °C

The distances of each peak angles from the pure δ-phase Bi_2O_3 peaks were calculated and given in Tables 2 and 3. As an example, the shifts in the peak positions of 750 °C sintered δ-phase samples were given in Fig. 1c for $2\theta = 31^o - 34^o$. In this figure, the peak shift is clearly observed. All XRD scattering peaks of each sample ($2\theta_n$) shifted to the right. For a more detailed analysis of the peaks, the calculated peak shift data were analysed in Fig. 3. It can be seen that the peak shift value in degree unit increases with the increasing $2\theta_n$ values. The highest angles have high peak shift. There was a relationship between the total dopant rate and peak shift values (Fig. 3a). The peak shift increases as the total dopant rate increasing. It can be seen in Fig. 3a and at the vertical axes for each peak shift number. The highest peak shift is observed at the sample with the highest total dopant rate (38 mol%). Same statements were observed with all the other δ-phase samples. On the other hand, when the cation dopant is Ytterbium, the increasing amount of peak shift is more than when the cation dopant is Erbium (Table 2). The ionic radius of the Ytterbium is smaller than the Erbium ionic radius. It can be seen in the literature reviews, when the ionic radius of the additive decreases, the lattice parameter decreases and XRD patterns shift to the right and, when the additive radius increases, the lattice is expanded and XRD patterns shift to the left [20, 21]. In this study, it is seen in Table 1 that the shift of peaks due to the decreased lattice parameters. This change in the lattice parameters also points out the successful synthesis of ternary systems and substitution of dopant and host cations. Furthermore, the reason for the shifts in the peak position is thought to be due to stress and structural defects in the crystal structure [22]. In addition to this, higher sintering temperature cause a higher peak shift. Table 3 shows the $2\theta_{Bi}$ and $2\theta_n$ scattering angles taken from XRD-patterns of pure δ-phase Bi_2O_3 and δ-phase 8E10YbSB samples sintered at 700, 750 and 800 °C, respectively. Here, produced ternary system and literature are compared and determined the shift value between their XRD peak positions. The evaluation of the sintering temperature effect on the peak shift is seen in Fig. 3b. The shift value of the sintered at 800 °C higher than sintered at the 700 °C samples. At the same sintering temperature, when the peak shift number at the same time the peak number increase (so increasing of 2θ peak values), the peak shift values increase approximately too. The minimum shift is observed for the minimum peak angle for all three sintering temperatures.

The lattice parameters of δ-phase *x*E*y*YbSB samples are given in Table 1. The lattice constant of pure δ-Bi_2O_3 is 5.5250 Å [19] and 5.5160 Å for 20YbSB binary system [12]. It is reported that the lattice parameters range of δ-Bi_2O_3 type solid solutions as a function of the doping of Yb_2O_3 is 5.53–5.515 Å and decreased slightly with the increasing Yb_2O_3 content [12]. Also, similarly to M.J. Verkerk et al. [11], lattice constants of the specimens decrease with an

Table 2 Peak shift changing with the total dopant rate; the 2θ angles from the XRD pattern of 8EyYbSB and xE20YbSB samples sintered at 750 °C and their differences from δ-Bi_2O_3

Sample name		δ-Bi_2O_3	8E10YbSB		8E20YbSB		8E30YbSB		4E20YbSB		12E20YbSB	
Total dopant ratio (mol%)		0	18		28		38		24		22	
2θ values (°)		$2\theta_{Bi}$ (°) [25]	$2\theta_1$ (°)	$2\theta_1$-$2\theta_{Bi}$ (°)	$2\theta_2$ (°)	$2\theta_2$-$2\theta_{Bi}$ (°)	$2\theta_3$ (°)	$2\theta_3$-$2\theta_{Bi}$ (°)	$2\theta_4$ (°)	$2\theta_4$-$2\theta_{Bi}$ (°)	$2\theta_5$ (°)	$2\theta_5$-$2\theta_{Bi}$ (°)
Peak Shift No.	1	27.95	27.98	0.03	28.16	0.21	28.38	0.43	28.14	0.19	28.28	0.33
	2	32.39	32.44	0.05	32.64	0.25	32.9	0.51	32.58	0.19	32.74	0.35
	3	46.45	46.52	0.07	46.82	0.37	47.18	0.73	46.7	0.25	46.98	0.53
	4	55.08	55.20	0.12	55.54	0.46	55.98	0.9	55.38	0.3	55.7	0.62
	5	57.76	57.88	0.12	58.24	0.48	58.72	0.96	58.06	0.3	58.44	0.68
	6	67.79	68.08	0.29	68.38	0.59	68.96	1.17	68.16	0.37	68.6	0.81
	7	74.85	75.02	0.17	75.52	0.67	76.18	1.33	75.26	0.41	75.8	0.95
	8	77.15	77.42	0.27	77.86	0.71	78.54	1.39	77.56	0.41	78.12	0.97
	9	86.16	86.46	0.26	87	0.84	87.8	1.64	86.62	0.46	87.32	1.16

increase in the content of Er_2O_3 [7, 11]. As seen in the literature, the parameter ranges of the ternary system (Table 1 and Fig. 4) corresponds to the literature. As seen in Table 1, the pure and δ-phase Bismuth Oxide has the highest lattice parameters and lattice parameters of doped ternary systems are lower than this. In addition, the lattice parameter decreases independent from temperature with the increasing total dopant ratio (Fig. 4). The main reason is the ionic radius difference between dopant cations (Er^{3+} and Yb^{3+}) and host cation Bi^{3+}. The effective ionic radius of Er^{3+}, Yb^{3+} and Bi^{3+} are 0.890 Å, 0.868 Å and 1.030 Å for six coordinates, respectively [23] and the ionic radius of dopant cations are smaller than the Bi^{3+}. It is reported in the literature that the lattice parameter of doped δ-phase Bismuth Oxides increases with the increasing dopant ratio for the binary system for the small dopant rate [24, 25].

Table 3 Peak shift changing with the sintering temperature; the 2θ angles from XRD pattern of δ-8E10YbSB samples sintered at 700 °C, 750 °C and 800 °C and differences with δ-phase pure Bi_2O_3 peak angles

Peak Shift No.	δ-phase 8E10YbSB					
	700 °C		750 °C		800 °C	
	$2\theta_6$ (°)	$2\theta_6$-$2\theta_{Bi}$ (°)	$2\theta_1$ (°)	$2\theta_1$-$2\theta_{Bi}$ (°)	$2\theta_7$ (°)	$2\theta_7$-$2\theta_{Bi}$ (°)
1	27.96	0.01	27.98	0.03	28.02	0.07
2	32.42	0.03	32.44	0.05	32.48	0.09
3	46.52	0.07	46.52	0.07	46.58	0.13
4	55.20	0.12	55.20	0.12	55.26	0.18
5	57.86	0.10	57.88	0.12	57.92	0.16
6	67.96	0.17	68.08	0.29	68.12	0.33
7	75.02	0.17	75.16	0.31	75.12	0.27
8	77.32	0.17	77.42	0.27	77.44	0.29
9	86.42	0.26	86.46	0.30	86.46	0.30

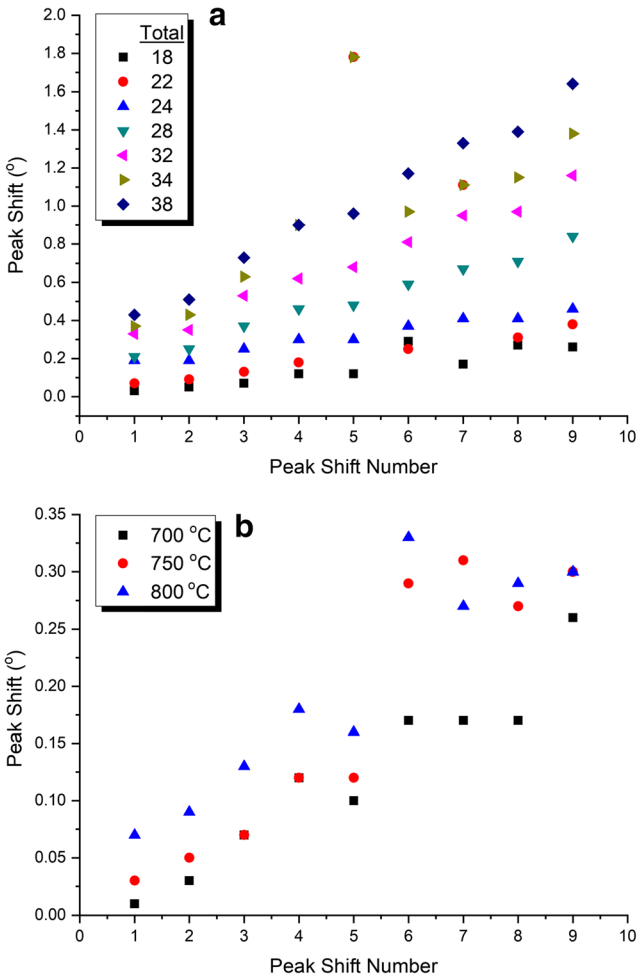

Fig. 3 Comparison between the peak shift degree and (**a**) the total dopant amount at 750 °C, (**b**) peak shift values at different temperatures

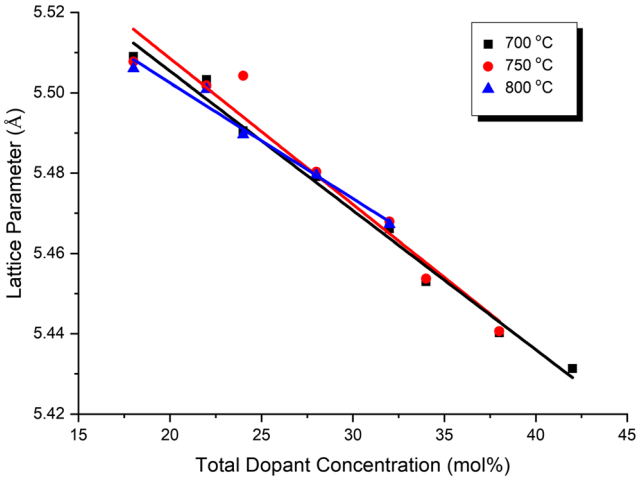

Fig. 4 Lattice parameters changing of the ternary system as a function of total dopant concentration annealed 48 h at 700, 750 and 800 °C

On the other hand, it is reported that the lattice parameter of δ-phase doped Bismuth Oxides decreases with the increasing dopant rate for the double or triple-doped systems and for the heavy doping rate [26, 27]. In samples produced this study, dopant rate is in heavy doping rate are limited compared with those in the literature. The amount of dopant cations with small ionic radius than Bi^{3+} increases, the lattice is shrunk through to lattice centre and lattice parameter is decreased. Therefore, as seen in Table 1, Er^{3+} doping causes shrinkage of the lattice and the lattice parameters decrease with the Erbium amount increases for the *x*E20YbSB systems. This behaviour of dopant effect on the lattice is also seen for Yb^{3+} dopant rate when Er^{3+} rate is fixed.

The burn-out temperature of additives is analysed with the TGA spectrogram in Fig. 5a and the mass loss of additives are seen in the graph. As seen in Fig. 5a, the additives in the non-sintered green powders are completely burned at ~620 °C and after then there was no decrease. The TG curve shows a mass loss of about 57.5 wt.% at a temperature range of 0–620 °C. According to the graph, the mass loss between 500 °C and 600 °C is about 2 wt.%. Also, as seen in Fig. 5b, the mass loss for the sintered sample is approximately 1.2 wt.%, which may be considered to physical water loss at a normal rate. Also, as seen in Fig. 5c, an endothermic peak is observed at about 700 °C. These peaks are point out to a phase transformation from the cubic phase at any phase.

The pressure effect on the microstructure is seen in Fig.6. In Fig.6, the three samples are seen pressed at 20 MPa, 75 MPa and 100 MPa pressure for 8E20YbSB samples sintered at 800 °C. The high pressure has been a positive effect on grain structure for the studied chemical compositions in this study. There is a limit value of pressure for the formation of grains, but the applied pressure as 100 MPa is quite suitable. The samples pressed at 100 MPa pressure, the grain formation was more quality, grain boundaries were seen clearly, and pores were disappeared when comparing with the

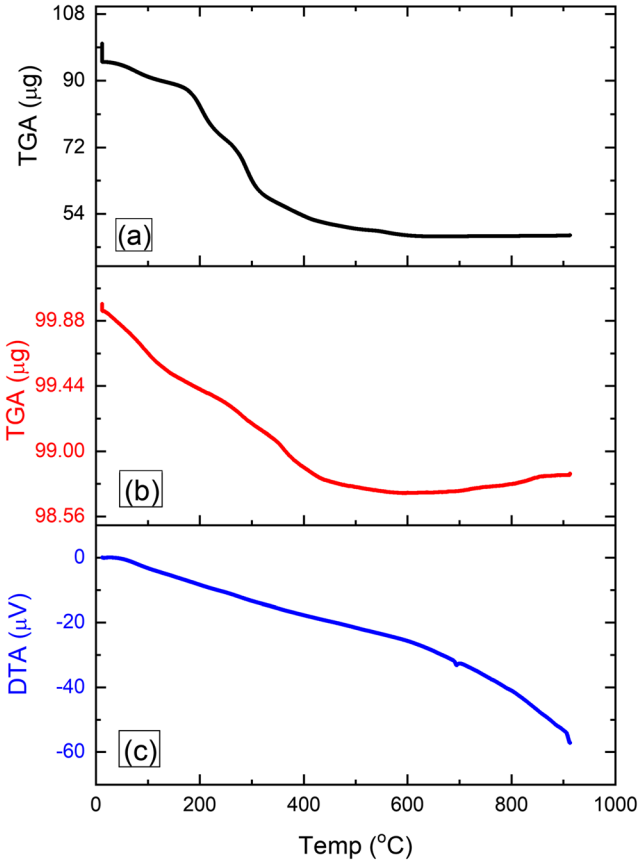

Fig. 5 TGA curves of burned green pellet at (**a**) 500 °C and (**b**) 800 °C and, (**c**) DTA curves sintered at 800 °C of 12E30YbSB sample

samples pressing at lower pressure. The grains are very important for high conductivity. Pore and small grain cause low conductivity. Because the charge carriers migrate through the crystal lattice and grain boundaries behave as a barrier for the migrant carriers. If the grain is big, the charge carriers migrate in the lattice without any scattering.

3.2 Conductivity characterization

The voltage and current data are obtained by4PPT for calculating the resistance R_{tot}. The total electrical conductivities (σ_{tot}) of pellets were calculated (Eq. 1) from the resistance values using with the Geometric Resistivity Correction Factor (*G*) (Eq.2).

$$\sigma_{tot} = \frac{I}{V}\frac{1}{G} \tag{1}$$

$$G = 2\pi s F_1(t/s) F_2(d/s) \tag{2}$$

In Eq. 2, *s*, *t* and *d* geometrical parameters point to the distances between probes, thickness and diameter of samples,

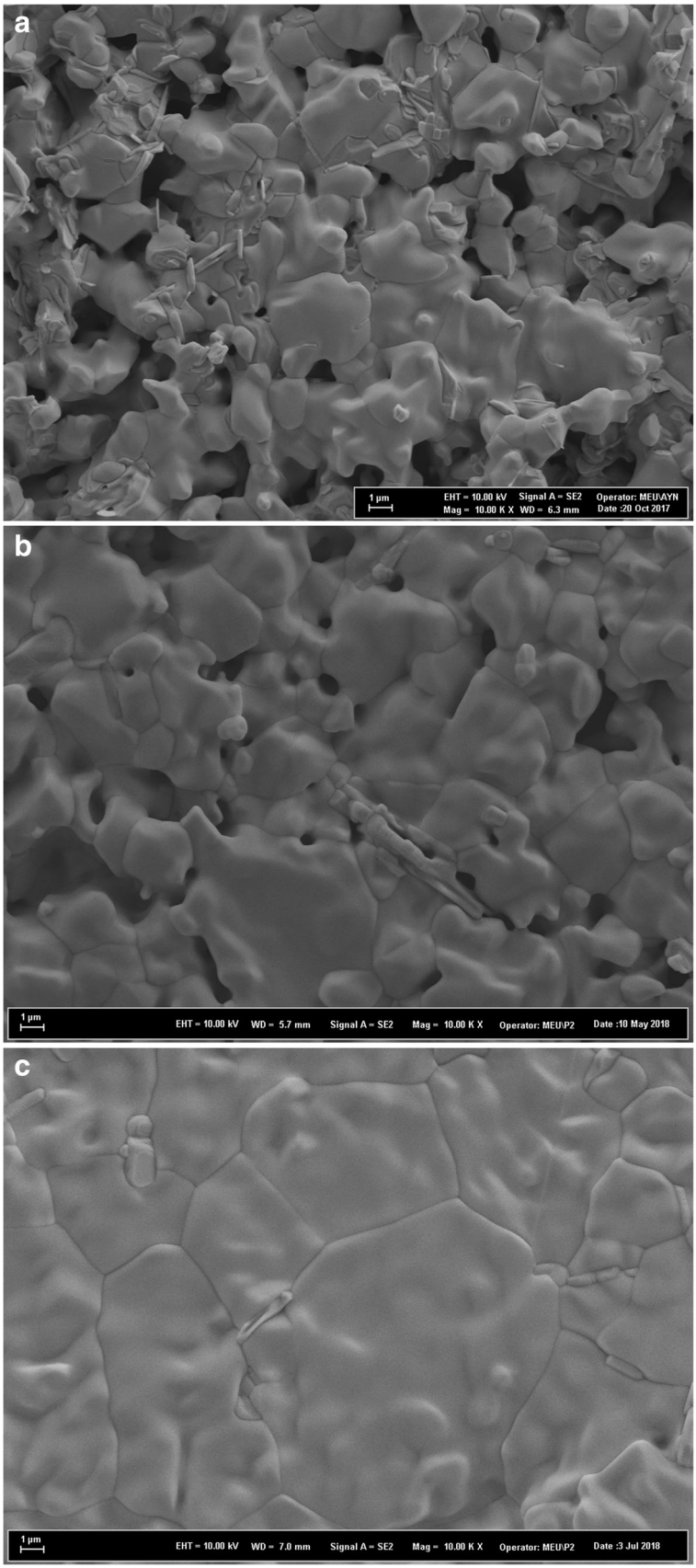

Fig. 6 SEM micrographs of 8E20YbSB ternary system ground with ball-mill and pressed at (**a**) 20 MPa (**b**) 75 MPa and (**c**) 100 MPa

respectively in centimetre unit. F_1(t/s) and F_2(d/s) functions are the effects on the conductivity of the thickness and diameter of the sample, respectively. The G function includes s, t and d parameters and determines the geometry effect of the sample on the conductivity. The experiment setup and detailed theoretical explanations of total conductivities with G were reported in our previous studies [28, 29]. Temperature dependence of the conductivity of electroceramic materials is expressed by the Eq. 3. In this expression, σ_0 is the pre-exponential factor, E_a is the activation energy for this thermally activated process and k is the Boltzmann's constant.

$$\sigma_{tot} = \sigma_0 e^{(-E_a/kT)} \tag{3}$$

The logarithmic electrical conductivities of the samples were plotted against the reciprocal temperatures. There were two types of characteristic curve observed all samples and these differences result in the crystal formation differences. These two types are seen in Fig. 7 for 4E20YbSB (Type I) and 4E30YbSB (Type II) samples. The plots of other samples were quite similar to the curves of these. The samples which have been Type I are $(x;y) = (4;20)$, (8;10), (8;20), (12;10), (12;30) and Type II are $(x;y) = (4;30)$, (8;30), (12;20) doping rate. Difference between the two types of graphics, Type I curve consist of two different temperature regions; the high-temperature region and the low-temperature (can also be called as the single-phase temperature) region.

The phase transition temperatures of samples were determined by analysis of these regions in the conductivity plots. The crystal structure and phase in the low-temperature region differ from the high-temperature region. The abrupt change in plot slope points to phase transition [24, 28]. The δ-phases is stable from room temperature to phase transformation temperature in the low-temperature region. The second single-phase occurs after the phase transformation and is known as high-temperature phase [28]. The second type in the other group seen in Fig. 7 (4E30YbSB) did not exhibit any phase after phase transition temperature. When the Yb dopant rate increase, the melting point of the ternary system increases, and phase transformation is delayed. The useful side of this, the stable δ-phase at room temperature remains stable up to the high-temperature region. In this case, higher conductivity values can be observed for δ-phase.

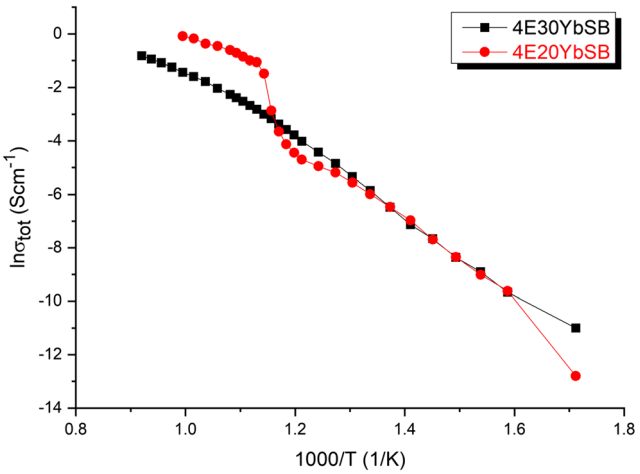

Fig. 7 Total conductivity versus temperature plots of 4E20YbSB and 4E30YbSB samples

The conductivity values of the δ-phase samples sintered at 700 °C are compared under two conditions called in the text as σ1 and σ2 and given in Table 4. In the first condition, the σ1 conductivity values at 510 °C ambient temperature for all δ-phase samples were compared with each other. This temperature is selected as it can be taken as a suitable degree for IT-SOFC operating temperature. In the second condition, the σ2 highest conductivity values in the low-temperature region were compared with each other in Table 4. In here, the data in the low-temperature region were only taken from the two-zoned graphs. Uncertainties of measurements (δ_x) for each conductivity values were calculated using with the experimental standard deviations and added to Table 4.

Increasing dopant rate causes the increase of the Oxygen defect in sub-lattice in Bismuth Oxide-based electroceramics [30]. In this case, the total conductivity also increases. On the other hand, there is limited value for the increasing of the total conductivity. On the contrary, as the conductivity increases after a limit dopant rate, the conductivity may start to decrease. In this highly dope condition, the scattering mechanism of drifted ions in lattice may become dominant and conductivity may be observed at low values. Conductivity values that are highly low for the total dopant rate are 38 mol% and 42 mol% and these are the highest total rates at the 510 °C ambient temperature (Fig. 8). The lowest conductivity value in both low-temperature region and at 510 °C ambient temperature is obtained for the 12E10YbSB sample with 42 mol% dopant, which is the highest dopant ratio. Since the lattice structure formation was dominant the conductivity abruptly decreased at 42 mol% due to the very high dopant rate. On the other hand, the 8E30YbSB sample has the highest conductivity value with 38 mol% total dopant rates in the low-temperature region. Furthermore, if the graph is analysed it can be seen that the phase transition is delayed and occurred at higher temperature with the increasing dopant ratio and the higher conductivity values are also observed (Fig. 8).

The Activation Energies of samples were calculated from Arrhenius plots drawing $\ln\sigma_{tot}$-$10^3/T$ graphs. The calculated activation energies of δ-phase samples sintered at 700 °C and this can be seen in Table 4 and all of them have around ~1 eV. An increase is seen at Activation Energies when Yb rate increases and Er dopant rate is constant. On the other hand, the opposite condition is not clearly seen. That the Er dopant rate is very low against the Yb dopant rate can be thought as a reason for this.

Table 4 The comparing the total conductivities and activation energies of δ-phase samples sintered at 700 °C

Sample	Total Dopant Rate (mol%)	G	σ1 (10^{-2} Scm^{-1})	$\delta_{\bar{x}}$ (±)	σ2 (10^{-2} Scm^{-1})	$\delta_{\bar{x}}$ (±)	E_a (eV)
8E10YbSB	18	0.384008	0.61	9.17E-06	0.61	9.17E-06	0.9
12E10YbSB	22	0.383239	1.32	5.31E-05	1.32	5.31E-05	1.2
4E20YbSB	24	0.384008	0.71	1.39E-05	2.61	1.01E-05	1.0
8E20YbSB	28	0.384008	1.29	8.06E-04	1.29	8.06E-04	1.0
12E20YbSB	32	0.386272	0.86	4.74E-05	11.02	9.24E-05	1.2
4E30YbSB	34	0.386272	0.79	1.14E-04	10.45	6.71E-05	1.3
8E30YbSB	38	0.386272	0.36	2.41E-05	12.16	3.60E-05	1.2
12E30YbSB	42	0.383239	0.18	2.86E-05	0.27	1.87E-05	1.0

4 Conclusion

Polycrystalline powders of $(Er_2O_3)_x(Yb_2O_3)_y(Bi_2O_3)_{1-x-y}$ ternary compounds were prepared under identical conditions via the sol–gel-based Pechini method. The crystal, microstructural, thermal, and electrical analysis is performed to δ-phase ternary systems (δ-*x*E*y*YbSB). According to the results of crystal analysis, the minimum sintering temperature should be at 700 °C for 48 h to obtain δ-phase ternary systems. The reason for low sintering temperature is the advantage of the Pechini method and the high sintering temperature is a negative effect for crystal structure formation. The lattice parameter decreases independent from the temperature with an increasing total dopant ratio. Total dopant rate should be minimum 18 mol% and more to obtain cubic phase for *x*E*y*YbSB ternary system. According to these results, the Er^{3+} dopant rate should be increased while the Yb^{3+} rate is decreasing, and the total doping rate should be constant at a certain ratio to obtain fcc-phases. In this ternary system, as the ionic radius of the doped material decreases, the lattice parameter decreases. This causes a shift to the right in XRD patterns. It was also thought that mixing the samples with ball mill caused stress and strains in the lattice and caused shifts in XRD patterns. The conductivity plots are exhibited as Arrhenius behaviour. The thermal activation energies are calculated from these graphs and the energy values are obtained ~0.9–1.3 eV. The minimum conductivity values are measured for the maximum dopant rate. The phase transition temperature from cubic to any phase increases with the increasing Yb dopant rate.

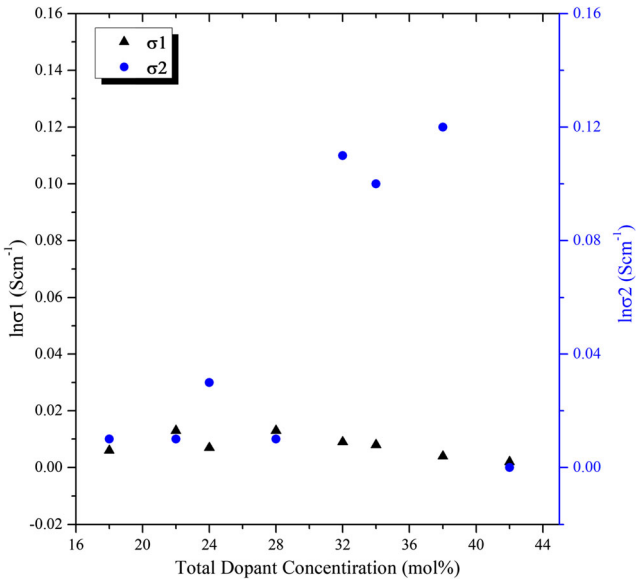

Fig. 8 The changing of total conductivities vs. total dopant concentration (**a**) σ1 at 510 °C ambient temperature (12E10YbSB) and (**b**) σ1 at the low-temperature region for stable δ–phase structure (8E30YbSB)

Acknowledgements The authors would like thanks to Mersin University for their financial support (Grant No. 2017-2-TP2-2434 and 2016-2-TP3-1957).

References

1. N. Jiang, E.D. Wachsman, Structural stability and conductivity of phase-stabilized cubic bismuth oxides. J. Am. Ceram. Soc. **82**(11), 3057–3064 (2004). https://doi.org/10.1111/j.1151-2916.1999.tb02202.x
2. N. Jaiswal, B. Gupta, D. Kumar, O. Parkash, Effect of addition of erbium stabilized bismuth oxide on the conductivity of lanthanum doped ceria solid electrolyte for IT-SOFCs. J. Alloys Compd. **633**, 174–182 (2015). https://doi.org/10.1016/j.jallcom.2014.12.243
3. E.D. Wachsman, K.T. Lee, Lowering the temperature of solid oxide fuel cells. Science **334**(80), 935–939 (2011). https://doi.org/10.1126/science.1204090
4. M. Yashima, D. Ishimura, Crystal structure and disorder of the fast oxide-ion conductor cubic Bi2O3. Chem. Phys. Lett. **378**(3-4), 395–399 (2003). https://doi.org/10.1016/j.cplett.2003.07.014
5. H.A. Harwig, A.G. Gerards, Electrical properties of the α, β, γ, and δ phases of bismuth sesquioxide. J. Solid State Chem. **26**, 265–274 (1978). https://doi.org/10.1016/0022-4596(78)90161-5
6. A.A. Yaremchenko, V.V. Kharton, E.N. Naumovich, A.A. Tonoyan, Stability of δ-Bi2O3-based solid electrolytes. Mater.

Res. Bull. **35**(4), 515–520 (2000). https://doi.org/10.1016/S0025-5408(00)00237-3
7. G.H. Zhong, J.L. Wang, Z. Zeng, Ionic transport properties in doped δ-Bi2O3. J. Phys. Conf. Ser. **29**, 106–109 (2006). https://doi.org/10.1088/1742-6596/29/1/020
8. S. Yilmaz, B. Kavici, C. Celen, E. Yildiz, A. Gurbuz, Structure and conductivity characterization of new type ionic conductor stabilized bismuth oxide ternary systems. Chin. J. Phys. **56**(1), 362–373 (2018). https://doi.org/10.1016/j.cjph.2017.11.010
9. Y. Polat, M. Arı, Y. Dağdemir, M. Ari, Y. Dağdemir, Phase stability, thermal, electrical and structural properties of (Bi2O3)1−x−y(Sm2O3)x(CeO2)y electrolytes for solid oxide fuel cells. Phase Transit. **90**(4), 387–398 (2017). https://doi.org/10.1080/01411594.2016.1206899
10. M.J. Verkerk, G.M.H. van de Velde, A.J. Burggraaf, R.B. Helmholdt, Structure and ionic conductivity of Bi2O3 substituted with lanthanide oxides. J. Phys. Chem. Solids **43**(12), 1129–1136 (1982). https://doi.org/10.1016/0022-3697(82)90141-X
11. M.J. Verkerk, K. Keizer, A.J. Burggraaf, High oxygen ion conduction in sintered oxides of the Bi2O3-Er2O3 system. J. Appl. Electrochem. **10**(1), 81–90 (1980). https://doi.org/10.1007/BF00937342
12. H. Ozlu Torun, S. Cakar, E. Ersoy, O. Turkoglu, The bulk electrical conductivity properties of δ-Bi2O3 solid electrolyte system doped with Yb2O3. J. Therm. Anal. Calorim. **122**(2), 525–536 (2015). https://doi.org/10.1007/s10973-015-4785-8
13. M. P. Pechini, Method of preparing lead and alkaline earth titanates and niobates and coating methods using the same to form a capacitor. US Pat 3,330,697 1967:2
14. M.C. Steil, Densification of Yttria-stabilized zirconia. J. Electrochem. Soc. **144**(1), 390–398 (1997). https://doi.org/10.1149/1.1837416
15. A.E. Danks, S.R. Hall, Z. Schnepp, The evolution of "sol-gel" chemistry as a technique for materials synthesis. Mater Horizons **3**(2), 91–112 (2016). https://doi.org/10.1039/c5mh00260e
16. S.W. Kwon, P.S. Bin, G. Seo, S.T. Hwang, Preparation of lithium aluminate via polymeric precursor routes. J. Nucl. Mater. **257**(2), 172–179 (1998). https://doi.org/10.1016/S0022-3115(98)00442-5
17. Y. Zhang, Y. Yang, S. Tian, C. Liao, C. Yan, Sol-gel synthesis and electrical properties of (ZrO2)0.85(REO1.5)0.15 (RE = Sc, Y) solid solutions. J. Mater. Chem. **12**(2), 219–224 (2002). https://doi.org/10.1039/b106876h
18. Y. Zhang, A. Li, Z. Yan, G. Xu, C. Liao, C. Yan, (ZrO2)0.85(REO1.5)0.15 (RE=Sc, Y) solid solutions prepared via three Pechini-type gel routes: 1 - gel formation and calcination behaviors. J. Solid State Chem. **171**(1-2), 434–438 (2003). https://doi.org/10.1016/S0022-4596(02)00227-X
19. PDF Card No .: 00–027-0052 Quality : C 2018:54059
20. P. Barpanda, N. Recham, J.N. Chotard, K. Djellab, W. Walker, M. Armand, J.M. Tarascon, Structure and electrochemical properties of novel mixed Li(Fe 1-xMx)SO4F (M = co, Ni, Mn) phases fabricated by low temperature ionothermal synthesis. J. Mater. Chem. **20**(9), 1659–1668 (2010). https://doi.org/10.1039/b922063a
21. A. Nakrela, N. Benramdane, A. Bouzidi, Z. Kebbab, M. Medles, C. Mathieu, Site location of Al-dopant in ZnO lattice by exploiting the structural and optical characterisation of ZnO: Al thin films. Results Phys **6**, 133–138 (2016). https://doi.org/10.1016/j.rinp.2016.01.010
22. B. C., Elements of X-Ray Diffraction. 2nd. Addison-Wesley Publishing Company Inc.; 1978
23. R.D. Shannon, Revised effective ionic radii and systematic studies of interatomic distances in halides and chalcogenides. Acta Crystallogr Sect A **32**(5), 751–767 (1976). https://doi.org/10.1107/S0567739476001551
24. S. Yilmaz, O. Turkoglu, I. Belenli, Synthesis of β-phase (Bi2O3)1−x(Dy2O3)x (0.01 <x < 0.10) system andMeasurement of oxygen ionic conductivity. Res Lett Mater Sci **2007**, 1–5 (2007). https://doi.org/10.1155/2007/97204
25. M. Bozoklu, O. Turkoglu, S. YIlmaz, M. ArI, I. Belenli, Oxide ionic conductivity and crystallographic properties of tetragonal type Bi2O3-based solid electrolyte doped with ho 2O3. Mater. Sci. Technol. **26**(10), 1239–1247 (2010). https://doi.org/10.1179/174328409X441238
26. S. Yilmaz, E. Yildiz, B. Kavici, Fabrication, characterization, and performance of YbDSB ternary compounds for IT-SOFC applications. Int. J. Appl. Ceram. Technol. **14**(4), 550–561 (2017). https://doi.org/10.1111/ijac.12695
27. Y.E. Gönen, I. Ermiş, M. Ari, Electrical properties of triple-doped bismuth oxide electrolyte for solid oxide fuel cells. Phase Transit. **89**(11), 1129–1136 (2016). https://doi.org/10.1080/01411594.2016.1150471
28. S. Yilmaz, O. Turkoglu, I. Belenli, Measurement and properties of the oxide ionic conductivity of β-phase in the binary system of (Bi2O3)1−x(Sm2O3)x. Mater. Chem. Phys. **112**(2), 472–477 (2008). https://doi.org/10.1016/j.matchemphys.2008.06.002
29. S. Yilmaz, O. Turkoglu, M. Ari, I. Belenli, Electrical conductivity of the ionic conductor tetragonal (Bi2O3)1-x(Eu2O3)x. Cerâmica **57**(342), 185–192 (2011). https://doi.org/10.1590/S0366-69132011000200009
30. H.A. Harwig, J.W. Weenk, Phase relations in Bismuthsesquioxide. Zeitschrift Fur Anorg Und Allg Chemie **444**(1), 167–177 (1978). https://doi.org/10.1002/zaac.19784440119